catalysts

MDPI

Article

Waste Biomass Utilization for the Production of Adsorbent and Value-Added Products for Investigation of the Resultant Adsorption and Methanol Electro-Oxidation

Hala Mohamed [1], Abeer Enaiet Allah [2], Doaa Essam [2], Ahmed A. Farghali [1], Ahmed A. Allam [3,4], Sarah I. Othman [5], Abdalla Abdelwahab [6] and Rehab Mahmoud [2,*]

[1] Materials Science and Nanotechnology Department, Faculty of Postgraduate Studies for Advanced Sciences, Beni-Suef University, Beni-Suef 62511, Egypt
[2] Chemistry Department, Faculty of Science, Beni-Suef University, Beni-Suef 62511, Egypt
[3] Department of Zoology, Faculty of Science, Beni-Suef University, Beni-Suef 65211, Egypt
[4] Department of Biology, College of Science, Imam Mohammad Ibn Saud Islamic University, Riyadh 11623, Saudi Arabia
[5] Department of Biology, College of Science, Princess Nourah bint Abdulrahman University, P.O. Box 84428, Riyadh 11671, Saudi Arabia; sialothman@pnu.edu.sa
[6] Department of Chemistry, College of Sciences, University of Ha'il, Ha'il 81451, Saudi Arabia
* Correspondence: rehabkhaled@science.bsu.edu.eg

Abstract: Waste valorization is necessary in today's society to achieve a sustainable economy and prosperity. In this work, a novel approach to the waste valorization of cuttlebone was investigated. This material was ground and calcined at 900 °C for 5 h in an inert atmosphere. The resulting calcined cuttlebone (CCB) was characterized using XRD, SEM, FTIR, BET, TGA, Zetasizer, and potential methods. The main phases in the CCB were determined to be CaO, MgO, $Ca_3(PO_4)_2$, and residual carbon. CCB was investigated as an adsorbent for the removal of dye from simulated wastewater streams. The maximum adsorption capacities for rhodamine B and crystal violet dyes were estimated to be 519 and 921 mg/g, respectively. For both dyes, the Avrami model was the best-fit model for representing adsorption kinetics. The study of adsorbent regeneration for CV as a representative example involved the use of several chemical solvents. Ethanol solvent was shown to have the highest adsorbent regeneration method efficiency, reaching 65.20%. In addition, CCB was investigated for methanol electro-oxidation for energy generation. As the methanol concentration increased, the maximum current density produced by the CCB increased, reaching approximately 50 mA/cm^2. This work paves the way toward waste valorization of natural matter for sustainable production and consumption of material, as per the requirements of the circular economy principles.

Keywords: cuttlebone; waste valorization; adsorbent; methanol electro-oxidation

Citation: Mohamed, H.; Enaiet Allah, A.; Essam, D.; Farghali, A.A.; Allam, A.A.; Othman, S.I.; Abdelwahab, A.; Mahmoud, R. Waste Biomass Utilization for the Production of Adsorbent and Value-Added Products for Investigation of the Resultant Adsorption and Methanol Electro-Oxidation. *Catalysts* **2024**, *14*, 574. https://doi.org/10.3390/catal14090574

Academic Editor: Young-Woong Suh

Received: 28 July 2024
Revised: 15 August 2024
Accepted: 26 August 2024
Published: 29 August 2024

1. Introduction

The dyeing process, which includes sourcing, sizing, de-sizing, bleaching, mercerization, printing, tinting, and finishing methods, is a crucial step in the production of textiles [1]. Large amounts of wastewater contaminated with dyes are released by the textile industry as a consequence of washing colored or printed clothing. According to the literature, 450,000 tons (t) of industrial synthetic dyes is produced each year by 40,000 different companies [2]. Human health, vegetation, and aquatic life are all significantly impacted by the release of such large amounts containing substantial loads of various colors [3].

Cationic dyes have a relatively high tinctorial value (<1 mg L^{-1}) and are considerably more toxic than anionic dyes [4]. The most commonly used synthetic cationic dyes, rhodamine B (Rh) and crystal violet (CV), are the most toxic dyes detected in textile wastewater. Because of their great stability and non-biodegradability, they play a vital role as textile colorants in the textile industry [5]. These colors can result in eye infections, gastrointestinal system

infections, respiratory tract infections, and skin irritation [6]. They are classed as neurotoxic and carcinogenic. During their development and simulation, they may also pose a risk to humans and animals. Inhaling or consuming Rh and CV can be hazardous, and extended use can damage the thyroid and liver, as well as causing irritation to the eyes and skin [6].

Various methods have been employed to eliminate dyes from wastewater, such as membrane filtration, chemical oxidation, ion exchange, biodegradation, adsorption, and photocatalysis, encompassing physical, chemical, and biological strategies [7–13]. Although photocatalysis is an easy and effective way of removing dye pollution, its complications as a cost-intensive process that releases photocatalysts into the water system and is inactive at night have limited its applications [12,14].

The method of adsorption is considered to be one of the most efficient strategies in the elimination of dye pollutants from water, due to its cost-effectiveness, superior performance, adaptability, and user-friendly nature [13]. One crucial aspect of this procedure involves the advancement of high-capacity adsorbents. Numerous studies have been undertaken to explore the efficacy of nanoparticles in eliminating cationic dyes from wastewater. The creation of cost-effective, ecologically sound adsorbents possessing inexpensive rates and outstanding adsorption characteristics stands as a critical consideration. The sustainable component of waste, residuals, and industrial products provides a cost-effective and renewable source of biomass [15].

Because it is less expensive and easier to handle, has no negative effects on the environment, and even generates income, using a recyclable portion of biomass improves its management. Adsorbents based on biosources show promising methods of removing pollutants from aqueous solutions [16]. This approach is both economically feasible and more effective in eliminating a variety of pollutants. Effective waste biomass has been investigated by many workers, with good adsorption properties [17]. A significant amount of attention has previously been dedicated to biological cuttlefish bone (CB), with the objective of enhancing the sustainability of the materials' manufacture using low-cost secondary raw materials so as to prevent resource depletion [18]. As an inorganic material, CB can be calcined to produce calcium oxide, which has a variety of uses (e.g., in biomaterials for medication and bone implants) [19]. Such materials can find promising applications in several applied fields, such as environmental and energy-related applications [20]. For the former, the resulting oxides after calcination can be tested as adsorbents for different pollutants [21]. The cuttlefish, or Sepia officinalis, is a valuable marine food that can be consumed by humans. However, the marine food industry produces tons of cuttlefish bone as waste every day, leading to contaminated environments [22]. It produces 6000–8000 tons of waste annually, consisting of an organic film covering and a porous $CaCO_3$ matrix [23]. Organic pollutants can be adsorbed on this biological waste [24]. Additionally, the inorganic portion of cuttlefish bone contains trace amounts of magnesium, sodium, and strontium, in addition to calcium carbonate ($CaCO_3$) in the form of aragonite. These minerals are important components of the bone recovery procedure [25]. Cuttlefish bone powder's affordability, environmental friendliness, high availability, improved interconnectivity, and biocompatibility are its key benefits when preparing hydroxyapatite [26].

Potential has also been shown in a variety of applications, such as the synthesis of calcium phosphate and calcium oxide for biomedical and non-biomedical uses, like dye adsorption, the production of bio-calcium oxide for use in industrial furnaces, and the production of energy storage batteries [27].

The attainment of sustainable development principles necessitates additional inquiries into the reutilization and valorization of permanently exhausted adsorbents. Presently, the practice of repurposing spent adsorbents has surfaced as a central focus of research. Recently, several previous reports have investigated the use of oxides similar to those resulting from CB calcination, such as CaO and MgO, as adsorbents for different pollutants—such as methylene blue [28], Congo red [29], other dyes [13,30–34], heavy metals [35–40], nitrogen [41], phosphate [42–44], and fluoride [45]—from wastewater effluents. For the latter, such materials may find applications as supports for active materials that can be

used in both energy conversion and storage devices [46]. Similar oxides have already been investigated as supports for several energy-related applications, such as methanol fuel cells [47] and ethanol fuel cells [47–51]. Such support offers several advantages, such as ease of preparation and cost-effectiveness.

On the other hand, the current focus of global attention is directed towards environmentally friendly and sustainable energy generation, which stands as a paramount concern. Fuel cells have attracted considerable attention over other conventional energy storage methods due to their unique attributes, including cost-effectiveness, minimal emissions, and uncomplicated design [7,51]. Direct methanol fuel cells, or DMFCs, have the potential for usage in portable electronics and electric vehicles. The fuel methanol offers low operating temperatures, rapid startup, excellent energy efficiency, and simplicity of storage and transportation. The most popular metal for DMFC anode catalysts is platinum, owing to its exceptional electrocatalytic activity and extended stability in electrolyte solutions [52]. Nevertheless, platinum's electrocatalytic activity is decreased and it is easily contaminated by CO or other carbonaceous intermediates [53]. It has been determined that using spent adsorbents is one of the best ways to implement all aspects and strategies of a circular economy for sustainable development [54]. Utilization of waste provides an ecologically sustainable way to reduce the harmful effects of industrial and municipal waste [55]. Given the inability of industry to recover and utilize waste as a valuable resource for recycled materials, there is a logical argument for prioritizing the energy valorization of biomass over its disposal in landfills. This approach serves to encourage diversification of energy sources and diminish reliance on non-renewable external sources, as waste commonly contains significant amounts of energy [15,56]. Extracting metals from solid waste is considered to be a process that requires less energy compared to the traditional method of obtaining them from raw materials. The methodologies involved in these processes align well with the fundamental principles of the circular economy [15]. As a result, it is more crucial than ever to produce and use renewable energy, which is also a key strategy for achieving "carbon neutrality". Lately, there has been a significant increase in interest in biomass-based electrocatalyst materials for methanol oxidation [57,58]. Identifying an appropriate catalyst that can offer adequate current density at low voltages and lower costs is one of the issues that this solves for the electrochemistry field. Many biomass-based electrocatalysts are superior because of their low cost, large electrochemically active surface area, flexibility for further modification [59,60], and enhanced electron transfer and reactant mass transport [60,61].

Based on the previous discussion, CB was chosen, and a thermal treatment was applied where CB was calcined at high temperatures for a specific time duration as an approach to produce calcined CB (CCB) and investigate its properties for the aforementioned applications. This is the first study to apply such a thermal treatment process for cuttlebone and to investigate the use of the resulting material in all such applications. The aims of this study were to investigate calcined CB's potential as an adsorbent and electro-oxidation catalyst.

2. Results and Discussion

This section is divided into three main subsections: The first is where the characterization of CCB is presented. In the following subsection, an adsorption study to investigate the adsorptive efficiency and performance of these materials is presented. Next, the methanol electro-oxidation results are discussed.

2.1. Cuttlebone Characterization

2.1.1. Morphological Analysis

Figure 1a,b show the SEM images of the calcined cuttlebone (CCB) material at various magnifications. Lamellar wall structures of CB that were not completely calcined are visible in the SEM images, as indicated by the red arrows [62]. They measured 2000–2500 nm in length and 600–750 nm in width. The lamellar wall is covered with 200–250 nm diameter spheres that are widely distributed. The spherical forms are the CaO and MgO that were

obtained from the calcined $CaCO_3$ and $MgCO_3$ in CB [19,63,64]. At higher magnification, as shown in Figure 1b, particulates or granules with different sizes and surface characteristics may be seen as tricalcium phosphate—the prototypical TCP that is probably formed from the interaction of CaO with phosphorus [63–65]. Depending on the composition of the crystal lattice and the ways in which calcium and phosphate ions interact, the surface may seem irregular or rigid.

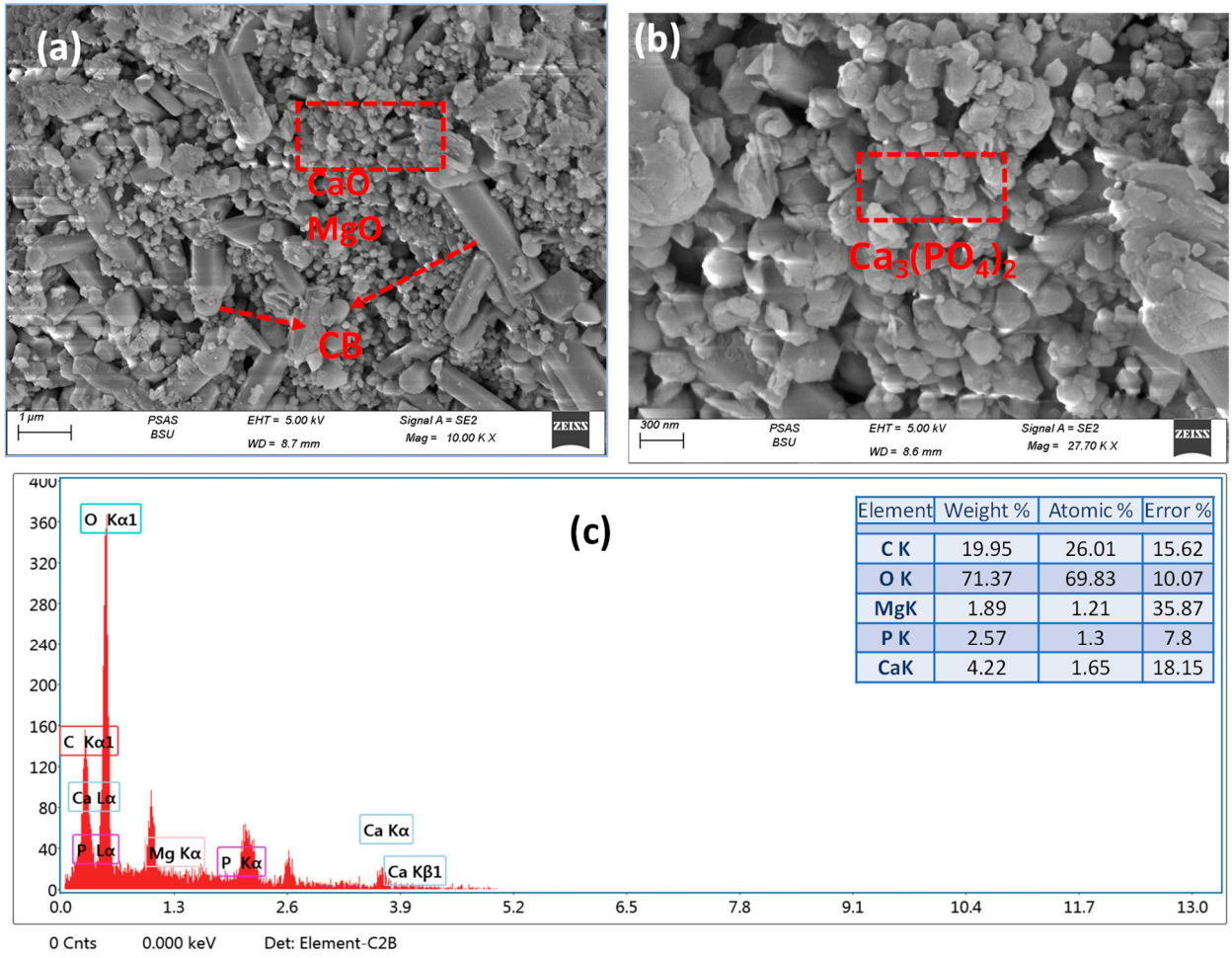

Element	Weight %	Atomic %	Error %
C K	19.95	26.01	15.62
O K	71.37	69.83	10.07
MgK	1.89	1.21	35.87
P K	2.57	1.3	7.8
CaK	4.22	1.65	18.15

Figure 1. (**a**,**b**) SEM micrographs at different magnifications and (**c**) EDX data of the CCB.

Ca, Mg, P, O, and C are present in the CCB structure according to the EDX data. Ca and Mg may originate from the calcium and magnesium carbonate included in the raw material. The carbon material that was obtained was attributed to carbon formed after calcining the organic components of CB in an inert atmosphere. Substance-based phosphorus (such as $Ca_3(PO_4)_2$) may be the origin of the phosphorous signal in Figure 1c, as further discussed by the XRD analysis below [63].

2.1.2. X-ray Diffraction (XRD)

X-ray diffraction (XRD) is an effective analytical technique for identifying the structural characteristics of a material. The XRD pattern of CCB is displayed in Figure 2a. The CCB material has significant crystalline structure characteristics, supporting the SEM morphology. According to the literature and JCPDS card numbers, the XRD patterns of CCB reveal three distinct crystalline phases: First, 2θ = 18.4°, 23°, 29.5°, 34.2°, 36°, 39.8°, 44.5°, 47.6°, 48.4°, 50.9°, 57.4°, and 65.6° correspond to the (113), (116), (300), (220), (131), (1 0 16), (048), (238), (416), (502), (428), and (0 5 16) planes of $Ca_3(PO_4)_2$, respectively, based on JCPDS card no. 009-0169 [66,67]. According to JCPDS card nos. 001-1160 and 00-37-1497,

the 2θ values of 32°, 54.2°, and 64.6° correspond to the (111), (220), and (311) planes of CaO, respectively [19]. The MgO crystalline structure shows peaks at 2θ = 43.3° and 62.4°, corresponding to the (200) and (220) planes, respectively (JCPDS card no. 003-0998) [68,69]. No broad peak was observed for carbon formed during calcination in an inert atmosphere originating from natural organic constituents within the original CB material, probably due to its low content.

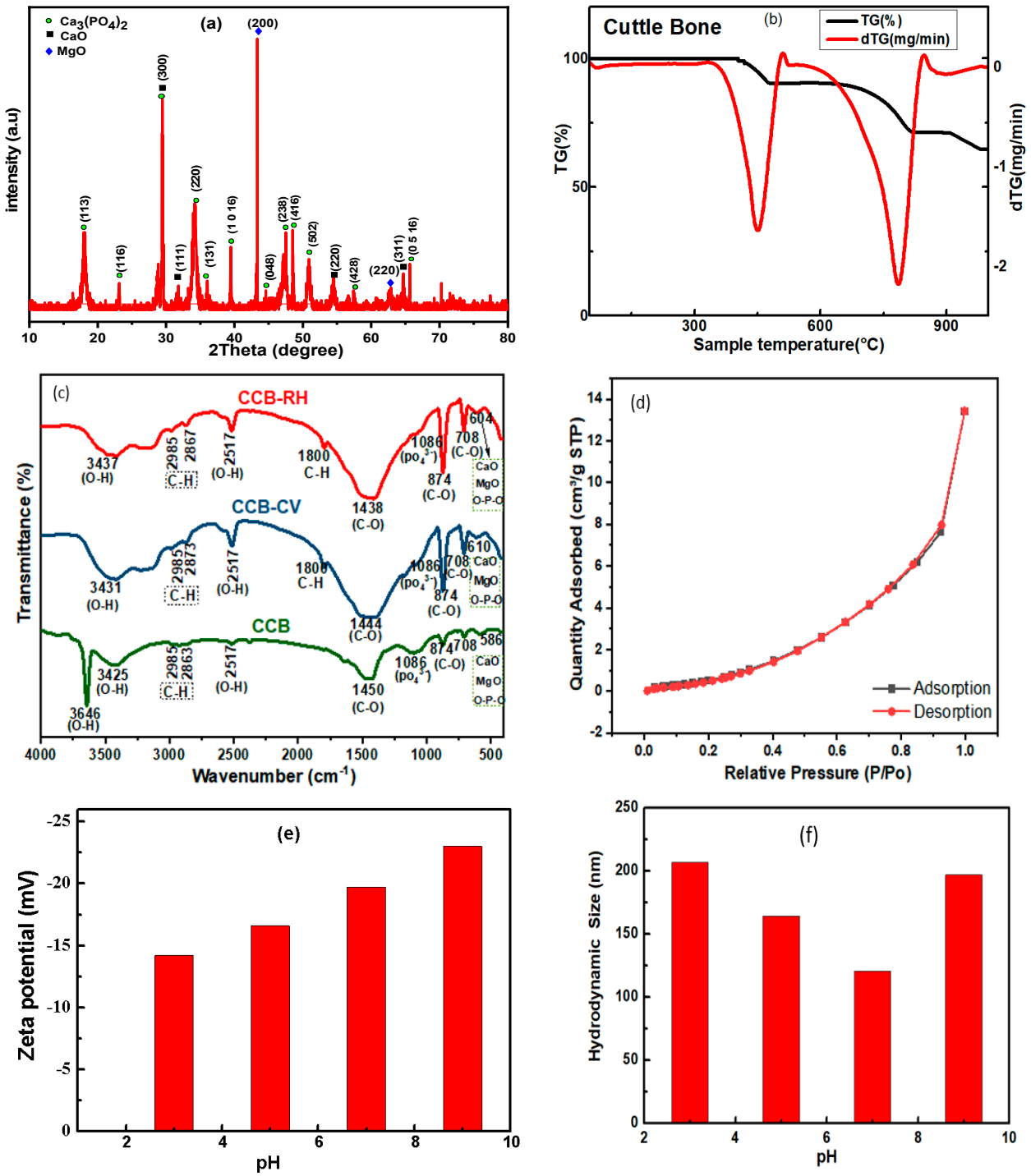

Figure 2. (**a**) X-ray diffraction and (**b**) TGA of CCB; (**c**) FTIR analysis of CCB (green), CCB-CV (blue), and CCB-RH (red); (**d**) N_2 adsorption–desorption isotherms of CCB; (**e**) zeta potential and (**f**) hydrodynamic particle size of CCB.

To determine a material's crystallite size, the Debye–Scherrer equation is frequently used along with XRD data. The figure illustrates how the crystallite size (Cz) is related to the Bragg angle (θ), the X-ray wavelength (λ), and a constant (K) and full width at half-maximum (β) [70]. The equation is as follows:

$$Cz = K\lambda/(\beta\cos(\theta))$$

The CCB peak at 2θ = 43.3° was the most intense and was 349.28 nm in size.

2.1.3. Thermogravimetric Analysis

Figure 2b displays the TGA results for CB. Two steps were taken to accomplish the thermal deterioration of CB: The organic composites of the raw materials, such as chitin, underwent decomposition during the first weight loss step, which accounted for approximately 10% of the weight loss and occurred between 400 and 480 °C [28]. The second weight loss stage, which accounted for 19.2% of the weight loss and occurred between 620 and 820 °C, was caused by the breakdown of $CaCO_3$ into calcium oxide (CaO) and carbon dioxide (CO_2) [28].

2.1.4. FTIR Analysis

The FTIR spectra of CCB, CCB-CV, and CCB-RH are shown in Figure 2c. For the CCB material, the strong band at 3646 cm^{-1} is attributed to the O–H group, confirming the presence of $Ca(OH)_2$ on the sample surface [71]. Moreover, the existence of a band at approximately 3642 cm^{-1} suggests that CaO was produced from $CaCO_3$ [72]. A broad band at approximately 3400 cm^{-1} generally indicates hydrogen-bonded hydroxyl group stretching [71]. The broadened absorption band at 3425 cm^{-1} reveals the presence of OH stretching vibrations. The broad and sharp bands between 3400 and 3600 cm^{-1} are identical to those bands of tricalcium phosphate reported in the literature [71]. The weak bands at 2985 and 2863 cm^{-1} are attributed to the existence of C–H bonding in the calcined material. The band at 2517 cm^{-1} corresponds to the accessibility of O–H stretching in uncalcined materials, and C–H asymmetric stretching of the amide appeared at 1800 cm^{-1} [71]. The (PO_4^{3-}) bending vibrations are shown by the band at 1086 cm^{-1} [73]. C–O stretching bands of carbonates are indicated at 708, 874, and 1450 cm^{-1} [19,74]. These carbonate signals originate from atmospheric CO_2, which carbonates the calcium phosphate phase [75]. Moreover, the slight decrease in the peak at 586 cm^{-1} may be a result of the production of CaO, MgO, and O–P–O bonds in (PO_4^{3-}) molecules [71,73,76]. The FTIR results after adsorption will be discussed later.

2.1.5. Textural Properties

The specific surface area (S_{BET}), pore volume, and pore diameter of the CCB were estimated using N_2 adsorption–desorption isotherms at 77 °K. According to the IUPAC categorization, type IV is represented by distinctive isotherms with an S_{BET} of 8.232 $m^2 \cdot g^{-1}$ (Figure 2d) [77]. The pore volume and pore diameter were determined to be 0.019 $cm^3 \cdot g^{-1}$ and 22.2 nm, respectively. The mesoporous structure, reflected by pore sizes ranging from 2 to 50 nm, justifies the significant adsorption capacity of CCB [78,79].

2.1.6. Zeta Potential

Studies on zeta potential show that the synthetic material is stable. This measures how electrically charged particles in a solution are attracted to or repelled from one another (Figure 2e). The measured zeta potential of CCB was −19.7 mV at pH = 7, indicating good stability of the formed nanoparticles. Figure 3a shows that CCB has a negative charge over the full range of pH values (3–9). The hydrodynamic size distribution of CCB was found to be 120.6 nm at pH = 7, as shown in Figure 2f.

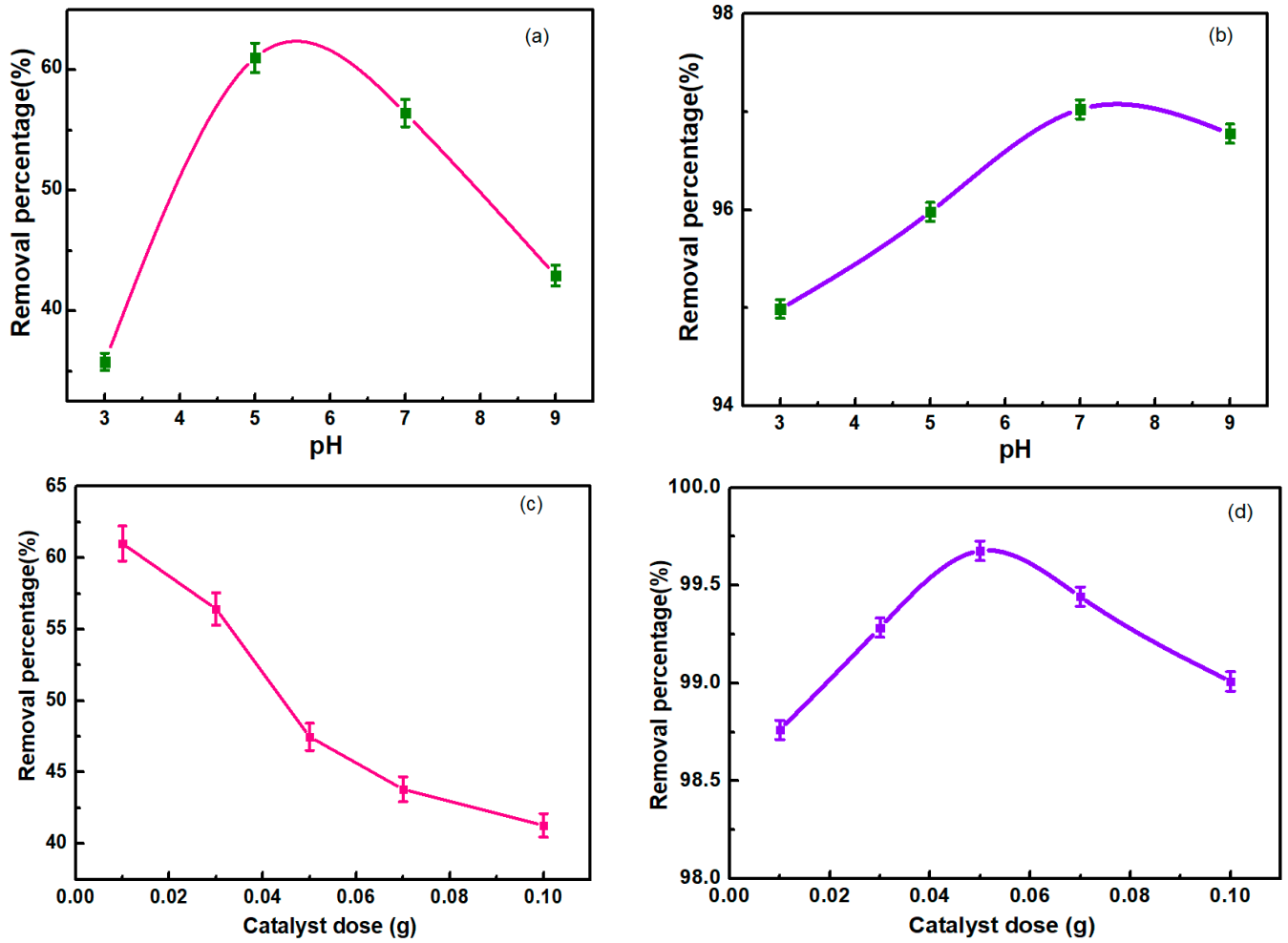

Figure 3. Effect of pH on the removal percentage of (**a**) RH and (**b**) CV, and the effect of catalyst dose on the removal percentage of (**c**) RH and (**d**) CV.

2.2. Adsorption Study

2.2.1. Effect of pH and Dose

The effect of pH on the adsorption of both RH and CV is illustrated in Figure 3a,b, respectively. As shown, the maximum removal percentage of RH occurred at pH 5. RhB is a zwitterionic dye that contains both positive and negative charges. The molecule is neutral at neutral pH because opposing charges cancel each other out. Nevertheless, under certain pH levels, these charges may become uneven and produce a positively or negatively charged molecule. The RhB molecules become cationic at pH levels around 5.0, allowing them to be attracted to the negatively charged CCB through electrostatic interactions, as the CCB's surface zeta potential was −15.8 mV. In comparison to basic pH, this advantageous interaction improves the adsorption process at acidic pH [80].

As shown in Figure 3b, the maximum RE% for CV occurred at pH = 7. CV is a cationic dye [81] that shows enhanced adsorption on negative surfaces, but even at pH = 9 the negative charge on CCB was greater (Figure 2e) and the RE% was lower. This can be attributed to the lower agglomeration state, as indicated by the lower hydrodynamic size (Figure 2f), compared to that at pH = 9. For RB, it can be concluded that the main factor affecting RE% is not the agglomeration state of CCB but, rather, hydrogen and other bonding where the dye body interacts with CCB. Such bonding (as discussed earlier in the FTIR section) may have a stronger effect on the RE% than simple electrostatic attraction and the adsorbent's agglomeration state. The optimal doses for RH and CV adsorption were measured to be 0.01 g and 0.05 g, respectively. As shown in Figure 3c,d, beyond the

optimal dose, lower values of RE% are calculated, possibly due to the agglomeration of the adsorbent. When the catalyst dose rises, the removal percentage of RH decreases due to agglomeration [82].

2.2.2. Adsorption Equilibrium Study

Several nonlinear isotherm models were investigated to fit the experimental results of CCB as an adsorbent for RH and CV. The models used were the Langmuir [83], Freundlich [84], Temkin, Dubinin–Radushkevich (D-R) [85], Langmuir–Freundlich, Sips [86], Toth [87], Redlich–Peterson [88,89], Baudu [90], and Fritz–Schlunder isotherms. For RH, the model that resulted in the highest R^2 value was the Fritz–Schlunder model (Figure 4a). The estimated parameters are tabulated in Table 1. The Fritz–Schlunder model is a five-parameter empirical mathematical isotherm model that was developed for single solute adsorption for a wide variety of applications [91]. This model can be considered to be a generalization of the Langmuir model and approaches its values when the exponents m_1 and m_2 both equal 1 [92]. For RH, the Langmuir model resulted in a maximum adsorption capacity of 519.029 mg/g over CCB. For CV, the maximum adsorption capacity was 921.12 mg/g, as shown in Table 1. The ability of the Langmuir model to fit the CV adsorption isotherm data (Figure 4b) reflects that CV adsorption occurs in a monolayer fashion over the surface of CCB.

2.2.3. Adsorption Kinetics Study

Figure 4c,d show the adsorption kinetics of RH and CV over CCB, respectively. For both dyes, the Avrami model showed the highest R^2 values (as shown in Table 2). This model is an empirical model that was first used to explain adsorption systems at the solid–solution interface [93]. The half-life of the adsorption process was calculated according to the equation shown in Table 2 [94] and was found to be 0.68 min^{-1} and 3.88 min^{-1} for RH and CV, respectively. The contact time required to attain 50% of the adsorption progress is known as the half-life. [94]. A fast equilibrium reaction is considered to be a key criterion for selecting an adsorbent material for real-life applications and engineering design [95]. These values suggest that CCB can be regarded as a promising adsorbent not only in terms of maximum equilibrium adsorption capacity but also in terms of the half-life of adsorption kinetics. In other words, CCB can be regarded as a fast adsorbent that allows the adsorption process to progress quickly.

2.2.4. Adsorption Mechanism

CCB showed promising maximum adsorption capacity for both RH and CV. As shown in Table 3, CCB shows very promising values of maximum adsorption capacity for both dyes compared to other similar materials in the literature. Even for materials that show higher performance, the cost of CCB is competitive compared to that of such materials. For instance, activated carbon costs between 0.5 and 132 USD/kg [96]. For CCB, the nitrogen required for calcination can be estimated to cost 15 USD per batch of furnace operation. The total energy requirements for 15, 12, and 5 h of running a ball mill, dryer, and furnace can be estimated to be 5.12 USD/25 g of the charge input to these devices, at a unit electricity cost of 0.16 USD/kWh. This results in a total cost of 800 USD/kg of CCB. This price could be lowered in future work by using less-costly inert gases such as carbon dioxide and relying on solar drying to reduce energy costs. For such promising adsorbents, insights into the adsorption mechanism are necessary to aid in the further development of their performance for real-life adsorption applications.

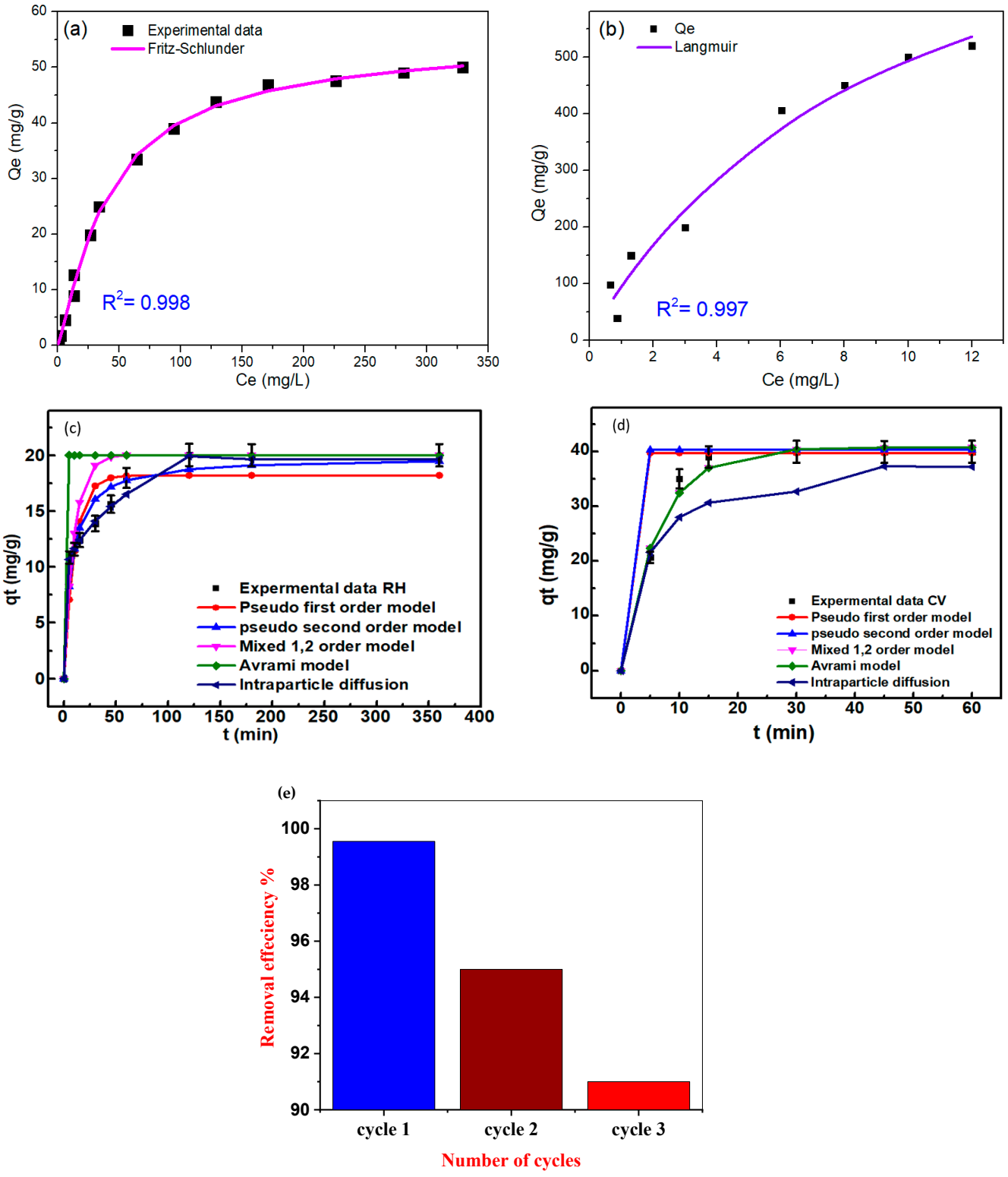

Figure 4. A best-fit model for adsorption isotherm data for (**a**) RH and (**b**) CV, kinetics of adsorption modeling for (**c**) RH and (**d**) CV on CCB, and (**e**) reuse of CCB for the CV adsorption.

Table 1. Nonlinear adsorption isotherm models.

Isotherm Models	Equation	Model Parameters		Values (RH)	R^2	Values (CV)	R^2
Two-parameter isotherms							
Langmuir	$q_e = \frac{q_{max} K_L C_e}{1+K_L C_e}$	q_{max} (mg/g)	Parameter that reflects monolayer formation	519.029	0.990	921.12	0.997
		K_L (L/mg)	Adsorption equilibrium constant	0.31		0.12	
Freundlich	$q_e = K_f C_e^{1/nf}$	K_f (L/g)	A constant of relative adsorption capacity	121.169	0.986	111.05	0.990
		$1/n_f$ (−)	Constant for surface heterogeneity	0.68		0.65	
Dubinin–Radushkevich	$q_e = (q_m) \exp(-K_{ad}\ \varepsilon^2)$ $\varepsilon = RT\ (1 + (1/C_e))$	q_m (mg/g)	Theoretical adsorption capacity	420.53	0.954	662.42	0.958
		K_{ad} (mol^2/KJ^2)	Constant related to adsorption energy	0.00036		0.00064	
Three-parameter isotherms							
Langmuir–Freundlich		q_{max} (mg/g)	Max. adsorption capacity	262.99	0.977	864.99	0.976
		K_{LF} (L/mg)	Equilibrium constant	0.918		0.13	
		β_{LF} (-)	Heterogeneity parameter	2.32		1.05	
Sips	$q_e = \frac{q_{max} K_S (C_e)^{n_s}}{1+K_S (C_e)^{n_s}}$	q_{max} (mg/g)	Maximum adsorption capacity	262.99	0.977	844.08	0.975
		Ks	Equilibrium constant (L/mg)	0.819		0.123	
		n_s (-)	Sips' model exponent	2.32		1.06	
Redlich–Peterson	$q_e = \frac{q_{max} C_e}{1+K_S (C_e)^{\beta_s}}$	q_{max} (L/mg)	Redlich isotherm constant	123.47	0.955	87.18	0.976
		K_s (mg/g)	Isotherm constant	0.0279		0.022	
		β_s (-)	Isotherm constant	2.68		1.54	
Khan	$q_e = \frac{Q_m b_K C_e}{[1+(b_K C_e)]^{a_k}}$	Q_m	Isotherm constant	95.81	0.997	1356.97	0.977
		b_K	Isotherm constant	0.01		0.08	
		a_k	Isotherm constant	1.27		1.35	
Toth	$q_e = \frac{K_e C_e}{\left[1+\left(K_L C_e\right)^n\right]^{\frac{1}{n}}}$	K_e (mol·L/mg^2)	Max. adsorption capacity	331.04	0.994	134.28	0.976
		K_L (L/mg)	Equilibrium constant	0.028		0.022	
		n (-)	Model exponent	2.68		1.54	
Higher-parameter isotherms							
Baudu	$q_e = \frac{q_{max} b_o (C_e)^{1+x+y}}{1+b_o (C_e)^{1+x}}$	q_{max} (mg/g)	Baudu max. adsorption capacity	132.31	0.992	11.047	0.963
		b_o (-)	Equilibrium constant	147,707.54		179,116.46	
		X (-)	Baudu parameter	0.58		0.649	
		Y (-)	Baudu parameter	14.67		1.53	

Table 1. *Cont.*

Isotherm Models	Equation	Model Parameters		Values (RH)	R^2	Values (CV)	R^2
Fritz–Schlunder	$q_e = \frac{q_{mFSS} K_1 (C_e)^{m_1}}{1 + K_2 (C_e)^{m_2}}$	q_{mFSS}	Fritz–Schlunder maximum adsorption capacity (mg/g)	5.23	0.998	249.02	0.979
		K_1	Model parameter	0.092		0.379	
		K_2	Model parameter	0.011		0.000163	
		m_1	Model parameter	1.299		0.8	
		m_2	Model parameter	1.26		3.09	

Table 2. Kinetics study models and their fitted parameters.

Kinetics Model	Kinetics Model Equation	Parameter	Values for (RH)	Values for (CV)
Pseudo-first-order	$q_t = q_e(1 - e^{-K_1 t})$ q_e is the adsorption capacity at equilibrium, k_1 is the pseudo-first-order rate constant (mg/g)	K_1 (min^{-1}) q_e R^2	1.86 20.44 0.95	1.86 39.74 0.96
Pseudo-second-order	$q_t = \frac{{q_e}^2 K_2 t}{1 + q_e K_2 t}$ k_2: pseudo-second-order rate constant (g/(mg·min))	K_2 q_e (mg/g) R^2	1.03 20.47 0.94	1.03 40.27 0.95
Mixed first- and second-order	$q_t = q_e \frac{1 - e^{-Kt}}{1 - f_2 e^{-Kt}}$ f_2: mixed 1st- and 2nd-order coefficient (g/(mg·min)) k: adsorption rate constant (min^{-1})	K q_e (mg/g) f_2 R^2	0.097 20.06 0.105 0.92	0.159 40.74 0 0.99
Avrami model	$q_t = q_e\left(1 - \left[e^{-K_{av} t}\right]^{n_{av}}\right)$ k_{av}: Avrami model rate constant n_{av}: model's component half-life = $(\frac{Ln\,2}{K_{av}})^{\frac{1}{n_{av}}}$	K_{av} (min^{-1}) n_{av} (-) q_e (mg/g) R^2	5.78 5.47 20.03 0.99	0.41 0.387 40.74 0.99

Table 3. Comparing maximum adsorption capacities for RH and CV over different adsorbents.

Material	Qmax. for RH (mg/g)	Reference	Material	Qmax. for CV (mg/g)	Reference
Activated carbon	2.5–1200	[97]			
CCB	519.029	This work	CCB	921.12	This work
Nanoporous polymers	260.42	[98]	Bentonite—alginate	601.9	[81]
Gelatin/activated carbon	256.41	[99]	Royal palm leaf sheath	454.54	[100]
Seeds of Aleurites Moluccana	178	[101]	Coconut husk powder	454.54	[102]
NiO nanoparticles	111	[103]	Khulays bentonite	263	[104]
Magnetic lignosulfonate	57.14	[105]	Magnetic nanoadsorbent	166.6	[106]
Modified *Volvariella volvacea*	33.51	[107]	*Citrus limetta* peel	81.48	[108]

The results from the FTIR spectra after adsorption can be very useful for obtaining insights into the possible interactions of RH and CV with CCB. The characteristic FTIR bands after the adsorption of crystal violet (CCB-CV) and rhodamine (CCB-RH) are also shown in Figure 2c. CCB-CV and CCB-RH showed the same characteristic bands as CCB, with some changes. The 3646 cm^{-1} band disappeared for both CCB-CV and CCB-RH, and

the O–H peak at 3425 cm^{-1} in CCB shifted to 3431 cm^{-1} in CCB-CV and 3437 cm^{-1} in CCB-RH, with a broader and more intense pattern. Compared to CCB-RH and CCB, the O–H group at 2517 cm^{-1} had greater broadening and intensity for CCB-CV. A characteristic C–H band that appeared at 1800 cm^{-1} in CCB-CV and CCB-RH indicated that the dye materials (CV and RH) and CCB material interact through hydrogen bonds. The C–O peaks at 1450, 874, and 708 cm^{-1} were more intense and broader than those of CCB, suggesting the existence of an adsorption interaction due to the carbonation of the phosphate phase. With additional distinguishing features, the metal oxide band at 586 cm^{-1} in CCB shifted to 610 and 604 for CCB-CV and CCB-RH, respectively. As shown in Figure 5, possible hydrogen bonding between hydrogen atoms in both dyes and oxygen in CaO, MgO, and $Ca_3(PO_4)_2$ could represent one of the main mechanisms for RH and CV adsorption over CCB.

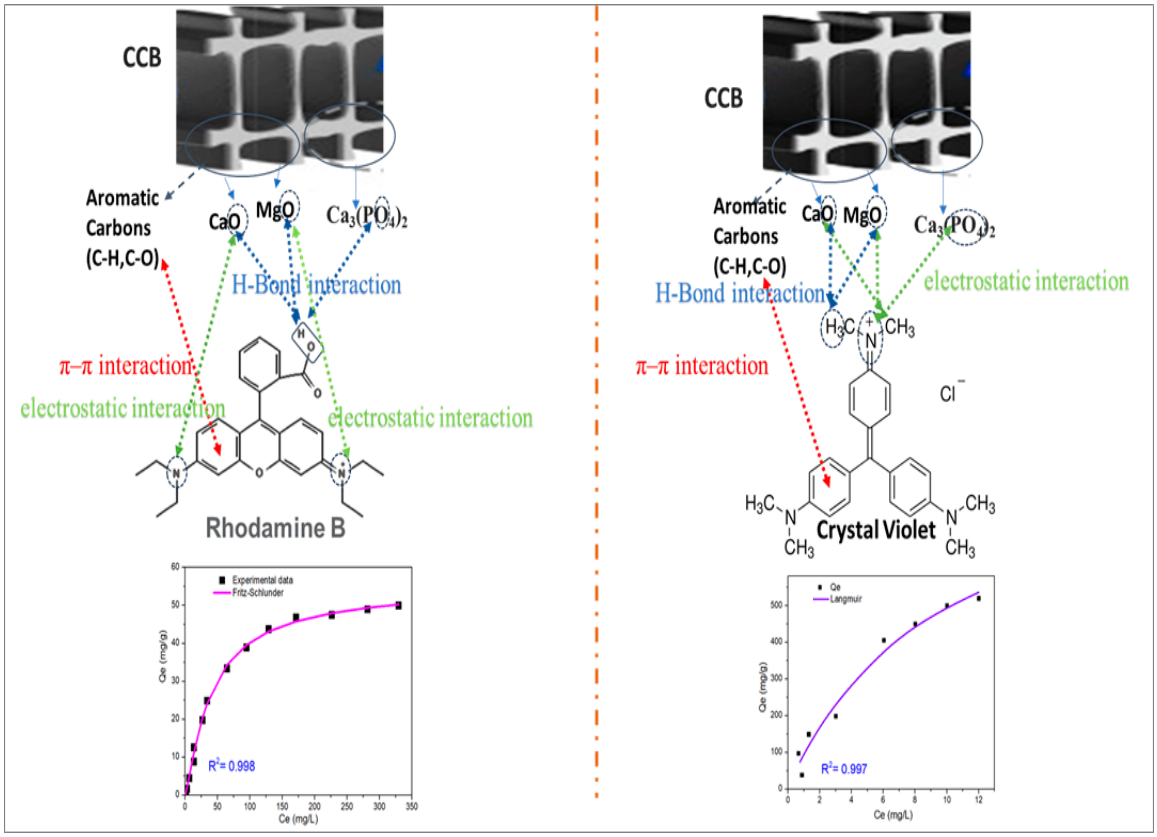

Figure 5. Possible interactions of RH and CV with the constituents of CCB during adsorption.

2.2.5. Reuse Study

Desorption and regeneration steps are required to investigate the applicability of a given adsorbent. If an adsorbent cannot be desorbed or regenerated effectively, the application value of the adsorbent is reduced, and it may create secondary environmental pollution. The desorption efficiency reached above 40% after 24 h using dimethyl formamide, 26.22% using acetone, and 5% using isopropanol. In addition, acetonitrile did not result in appreciable CV desorption, while methanol and ethanol showed desorption efficiencies of 55% and 65.20%, respectively. The eluent showing the highest desorption efficiency was ethanol, which reached 65.20%, probably due to the high solubility of CV in ethanol. Reuse of the adsorbent was conducted in ethanol, where almost no observable loss in removal efficiency was observed for three consecutive cycles, indicating the promising reusability of this adsorbent (Figure 4e).

2.3. Methanol Electrochemical Oxidation

One of the aims of this study was to investigate CCB as an electrocatalyst for methanol electro-oxidation. As shown in Figure 6a, as the methanol concentration increases, the maximum current density generated by CCB increases, reaching approximately 50 mA/cm^2 in 3 M methanol. As shown in Table 4, CCB can be regarded as a promising material compared to other nonmetallic waste catalysts reported in the literature, such as spent metal hydroxide catalysts. The performance of CCB may be further enhanced by using CCB as a support for state-of-the-art metal nanoparticles used for such applications. The electrochemical performance of CCB was assessed using cyclic voltammetry at scan rates of 5–60 mV/s between 0 and 0.6 V (vs. Ag/AgCl), as shown in Figure 6b. With increasing scan rate, the maximum produced current density increased. Figure 6c illustrates the relationship between the anodic peak current density and the square root of the scan rate. The linear relationship shows that the electrocatalytic oxidation of methanol over CCB is a diffusion-controlled process [109]. Moreover, it is important to investigate the stability of electrodes using techniques such as chronoamperometry (CA). The CA of the CCB is presented in Figure 6d, which shows that CCB possesses reasonable stability over 3600 s, with no significant deterioration in the electrochemical performance.

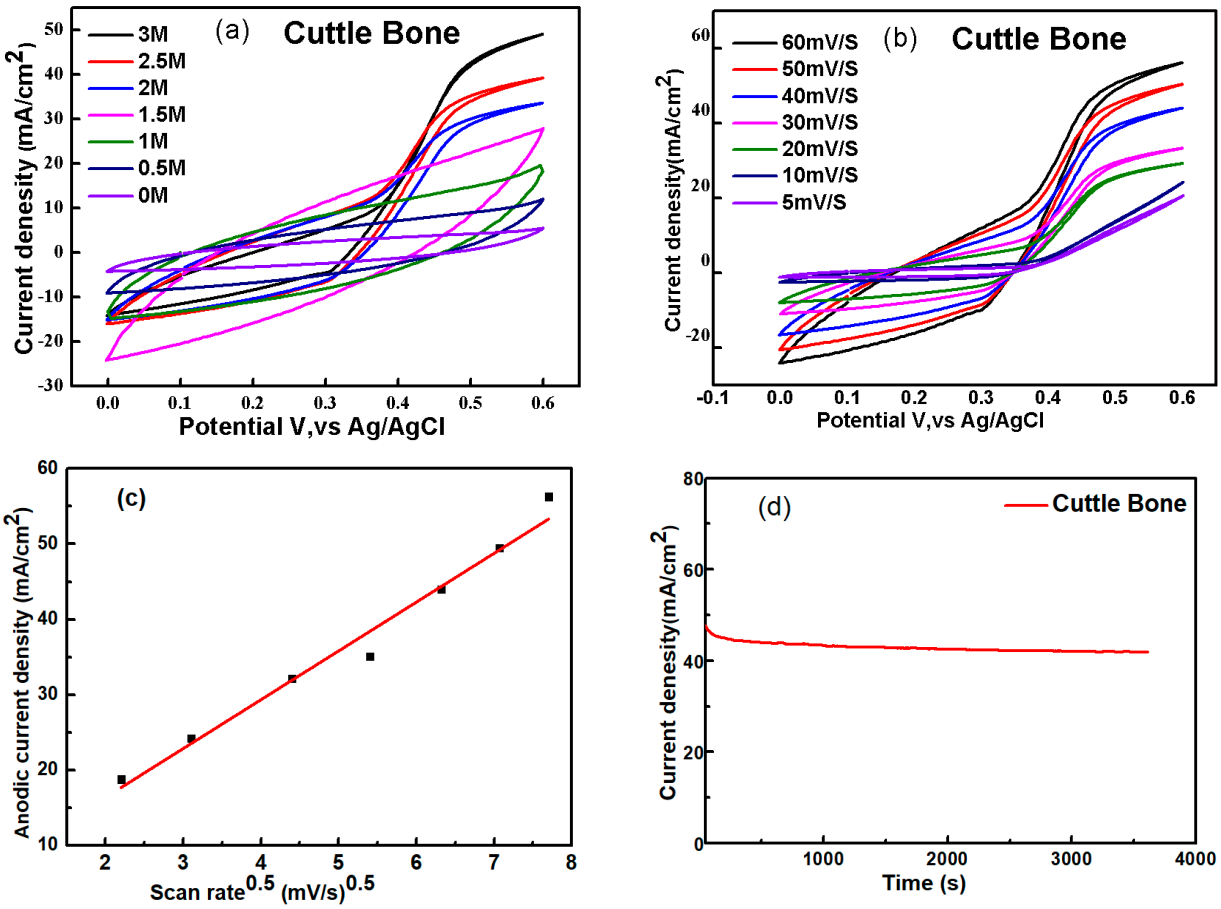

Figure 6. (**a**) Cyclic voltammograms of CCB in 1 M KOH at diverse methanol concentrations in a potential range of 0.0–0.6 V (vs. Ag/AgCl), and (**b**) CCB cyclic voltammograms in 1 M KOH in a potential range of 0–0.6 V (vs. Ag/AgCl); (**c**) a linear relationship between scan rates ~0.5 and the anodic peak current density, and (**d**) a chronoamperometric plot of the CCB at 0.6 V for 3600 s.

Table 4. Comparison of activity of electro-oxidation of methanol reported in this work with previous reported studies.

Material	Methanol Concentration (M)	Current Density (mA/cm^2)	Reference
CCB	3	50	This work
ZnMgFe LDH/ceftriaxone sodium	3	47.00	[110]
ZnCoFe LDH/oxytetracycline	1	20.00	[111]
ZnCoFe LDH/methylene blue	3	12.61	[82]
CoNiZnFe LDH/methyl orange	3	8.40	[109]

3. Materials and Methods

Cuttlebone (CB) was acquired from the Governorate of Alexandria, Egypt, while potassium hydroxide (KOH) (Oxford, Maharashtra, India) and sodium hydroxide (NaOH) were procured from Egyptian Piochem (Giza, Egypt) for the purpose of laboratory chemical utilization without the need for additional purification. Hydrochloric acid (HCl) was sourced from ECSA Chemicals (CarloErba reagents, Cairo, Egypt). Methanol was provided by ALPHA CHEMIKA (Mumbai, Maharashtra, India). Rhodamine B was utilized for microscopy (C.I.NO.45170, Loba Chemie PVT.LTD, Mumbai, India). Crystal Violet Extrapure was obtained from ALPHA CHEMIKA (Mumbai, Maharashtra, India).

3.1. Cuttlebone Collection

Marine waste cuttlefish bones were collected from a beach in Alexandria Governorate, Alexandria, Egypt.

3.2. Cuttlebone Thermal Treatment

The removal of odor and microorganisms necessitated the extraction and division of the carbon black into minute segments. Following this, the carbon black underwent a thorough rinsing with deionized water, a boiling process lasting ten minutes, and subsequent drying at a temperature of 100 °C for a duration of 12 h [112]. By utilizing a ball mill (photon ball mill), the carbon black was finely pulverized to create a powder. Subsequently, a pyrolysis procedure was conducted within a tube furnace under a nitrogen environment for a period of five hours at a temperature of 900 °C. Upon completion of the calcination process, the furnace was allowed to gradually return to room temperature. Prior to commencing the analytical assessment, the specimens were housed in a desiccator for storage purposes.

3.3. Material Characterization

The calcined cuttlebone (CCB) was characterized using a number of instruments: A PANalytical X-ray diffractometer (Empyrean, Almelo, The Netherlands) equipped with Cu-Kα radiation (wavelength of 0.154 nm, I = 35 mA, scanning at a rate of 8°/min, V = 40 kV) from a two-theta range of 5° to 80° was used to measure the crystallinity of the sample. To identify the functional groups between 400 and 4000 cm^{-1}, Fourier-transform infrared (FTIR) spectroscopy (Bruker-Vertex 70, KBr pellet technique, Berlin, Germany) was employed. Field-emission scanning electron microscopy (FESEM, ZEISS, Sigma 500 VP, Jena, Germany) was used to analyze the morphology of the CCB. CTX concentrations were tracked using a UV–VIS spectrophotometer (SHIMADZU UV-2600, Kyoto City, Japan). The pH of the solution was determined using an automatic surface pH meter (Adwa–AD1030, Szeged, Hungary). Using a Malvern Instruments Ltd. instrument (Malvern, UK), the hydrodynamic particle sizes and zeta potentials of the particles were also determined. Nitrogen adsorption–desorption isotherms were used to calculate the Brunauer–Emmett–Teller (BET) surface area, pore volume, and pore diameter (TriStar 3020, Micromeritics, Norcross, GA, USA). The thermal stability and phase transition of the prepared materials were investigated using a TGA/DTA device (Setaram Labsys Evo S60 analyzer, Caluire, France).

3.4. Adsorption Study

Experiments on batch adsorption were carried out at room temperature (25 °C). A dye stock solution containing 1000 mg (1000 ppm) was made and used for the subsequent dilutions. Using 50 mL Falcon tubes containing a predefined mass of the CCB adsorbent, the effects of pH were investigated. Using a pH meter (Metrohm 751 Titrino, Herisau, Switzerland), the pH was determined. Prepared solutions of 0.1 M HCl or 0.1 M NaOH were used to adjust it to the necessary value. We adjusted the pH of the solutions before beginning the work. Using a syringe fitted with a syringe filter (Millipore, Nylon, 0.22 mm pore size, Burlington, MA, USA), liquid samples were obtained. We used an orbital shaker to agitate the samples all night long. UV–VIS spectroscopy was used to measure the dyes' residual concentration. Equations (1) and (2) were used to compute the amount of dye adsorbed (q_e) and the removal percentage (RE%), respectively:

$$q_e = \frac{(C_o - C_t)V}{W} \quad (1)$$

$$\text{Removal percentage (RE\%)} = \frac{C_o - C_t}{C_o} \times 100 \quad (2)$$

where q_e is the amount of dye adsorbed per gram, and C_o and C_t are the initial concentration and the concentration after dye adsorption (mg/L) at time t (min), respectively. W is the mass of the adsorbent in grams, and V is the volume of the dye solution (liters). The effect of adsorbent dosage was investigated at a constant dye concentration (50 mg/L), while the dose of the adsorbent was varied from 0.01 g to 0.10 g. To investigate the adsorption isotherms, a range of initial dye concentrations, from 5 mg/L to 500 mg/L, were employed. In addition, many isotherm models were studied in an attempt to fit the adsorption data. Lastly, different kinetics models, including pseudo-first-order [113], pseudo-second-order [114], intraparticle diffusion [115], and Avrami [116], were fitted to the dye adsorption kinetics after they had been studied. For adsorbent recovery investigations, adsorbents such as ethanol, acetone, acetonitrile, isopropanol, dimethylformamide, methanol, and acetonitrile were utilized. Following the adsorption process, ten milligrams of adsorbent was combined with twenty-five milliliters of CV reagent. The samples were then agitated at 25 °C and 200 rpm for 24 h. The regeneration efficiency was determined using ultraviolet–visible spectrophotometry to quantify safinamide. Three regeneration cycles were implemented in the adsorbent reuse experiments.

3.5. Electrochemical Methanol Oxidation

An AUTOLAB PGSTAT 302 N (Metrohm, Herisau, Switzerland) potentiostat with NOVA 1.11 software was used to measure the electrocatalytic activity of CCB. Ag/AgCl and platinum electrodes fitted to three-compartment glass cells served as the reference and counter electrodes, respectively. Before use, fine alumina powder was used to clean the glassy carbon electrode (GCE), a cylindrical, white, mirror-like surface with a diameter of 3 mm and length of 500 mm (Autolab Metrohm, Switzerland). Subsequently, 400 µL of isopropanol and 15 µL of a 5-percent Nafion solution were used to gently sonicate a slurry containing 5 mg of CCB for thirty minutes at room temperature. Then, 10 µL of the sonicated suspension was applied to the active area of the GC electrode. The electrode surface was then dried for a final half-hour at 60 °C. Using a 1 M KOH electrolyte solution, the electrocatalytic activity of the generated electrodes was evaluated (with and without methanol). The cyclic voltammetry experiments involved a change in scanning rates from 5.0 to 60 $mV \cdot s^{-1}$. For 3600 s at 0.6 V, chronoamperometry (CA) measurements were conducted.

4. Conclusions

In this work, a simple method for the valorization of cuttlebone waste was implemented by employing thermal treatment of such waste material in an inert atmosphere

at elevated temperatures. CCB was produced in this study by heating the original dried and crushed material at 900 °C for 5 h. EDX analysis showed signals that reflected the presence of carbon, oxygen, calcium, magnesium, and phosphorous in the CCB structure. XRD analysis revealed the presence of CaO, MgO, and calcium phosphate phases as the main constituents of CCB. This shows that the original carbonate structure in the material before thermal treatment decomposed into the corresponding oxides and phosphates upon thermal treatment. In addition, organic constituents were converted to residual carbon due to the inert atmosphere used during thermal treatment. CCB was used as an adsorbent for the removal of dye from wastewater effluents. In terms of performance, CCB showed high adsorption capacity for both RH and CV dyes, indicating its promising future for possible use as a support for nanoadsorbents, or as a standalone adsorbent. The kinetics of adsorption indicated a fast half-life, reflecting its fast adsorption kinetics. As a methanol electro-oxidant, CCB has shown promising results and could be further enhanced upon possible compositing with electroactive nanomaterials. These results pave the way toward exploiting the possible uses of such materials as a standalone or upon compositing with nanomaterials for the waste valorization of natural inorganic wastes. The valorization of such materials facilitates the transition toward sustainable production and consumption to serve the principles of a circular economy.

Author Contributions: H.M. made contributions to the design, gathering, and analysis of the figures. A.E.A. helped with the design of experimental work, manuscript writing revision, and supervision. D.E. made contributions to the gathering and analysis of data. A.A.F. helped with the experimental work design, manuscript writing, and supervision revisions. A.A.A. made contributions to the interpretation and analysis of the data. S.I.O. made a design contribution to the study. A.A. made contributions to the design of the figures and to the writing and editing of the manuscript. R.M. helped with the planning of the experimental projects as well as the editing, writing, and supervision of the manuscript. All authors have read and agreed to the published version of the manuscript.

Funding: Princess Nourah bint Abdulrahman University Researchers Supporting Project number (PNURSP2024R5), Princess Nourah bint Abdulrahman University, Riyadh, Saudi Arabia.

Data Availability Statement: The datasets used and/or analyzed during the current study are available from the corresponding author upon reasonable request.

Conflicts of Interest: The authors declare no conflicts of interest.

References

1. Al-Gheethi, A.A.; Azhar, Q.M.; Kumar, P.S.; Yusuf, A.A.; Al-Buriahi, A.K.; Mohamed, R.M.S.R.; Al-Shaibani, M.M. Sustainable approaches for removing Rhodamine B dye using agricultural waste adsorbents: A review. *Chemosphere* **2022**, *287*, 132080. [CrossRef]
2. Forgacs, E.; Cserháti, T.; Oros, G. Removal of synthetic dyes from wastewaters: A review. *Environ. Int.* **2004**, *30*, 953–971. [CrossRef] [PubMed]
3. Fazal, T.; Mushtaq, A.; Rehman, F.; Khan, A.U.; Rashid, N.; Farooq, W.; Rehman, M.S.U.; Xu, J. Bioremediation of textile wastewater and successive biodiesel production using microalgae. *Renew. Sustain. Energy Rev.* **2018**, *82*, 3107–3126. [CrossRef]
4. Güzel, F.; Sayğılı, H.; Sayğılı, G.A.; Koyuncu, F. Decolorisation of aqueous crystal violet solution by a new nanoporous carbon: Equilibrium and kinetic approach. *J. Ind. Eng. Chem.* **2014**, *20*, 3375–3386. [CrossRef]
5. Rashid, N.; Rather, M.A.; Bhat, S.A.; Ingole, P.P.; Bhat, M.A. Highly efficient catalytic reductive degradation of Rhodamine-B over Palladium-reduced graphene oxide nanocomposite. *Chem. Phys. Lett.* **2020**, *754*, 137724. [CrossRef]
6. Zaher, A.; Kamal, W.; Essam, D.; Yousry, E.M.; Mahmoud, R. Repurposing Co-Fe LDH and Co-Fe LDH / Cellulose micro-adsorbents for sustainable energy generation in direct methanol fuel cells. *J. Water Process Eng.* **2024**, *62*, 105317. [CrossRef]
7. Faro, M.L.; Antonucci, V.; Antonucci, P.; Aricò, A. Fuel flexibility: A key challenge for SOFC technology. *Fuel* **2012**, *102*, 554–559. [CrossRef]
8. Kumar, A.; Rana, A.; Sharma, G.; Naushad, M.; Dhiman, P.; Kumari, A.; Stadler, F.J. Recent advances in nano-Fenton catalytic degradation of emerging pharmaceutical contaminants. *J. Mol. Liq.* **2019**, *290*, 111177. [CrossRef]
9. Bianchi, C.L.; Djellabi, R.; Della Pina, C.; Falletta, E. Doped-polyaniline based sorbents for the simultaneous removal of heavy metals and dyes from water: Unravelling the role of synthesis method and doping agent. *Chemosphere* **2021**, *286*, 131941. [CrossRef]
10. Rathi, B.S.; Kumar, P.S. Sustainable approach on the biodegradation of azo dyes: A short review. *Curr. Opin. Green Sustain. Chem.* **2021**, *33*, 100578. [CrossRef]

11. Abdulkhair, B.; Salih, M.; Modwi, A.; Adam, F.; Elamin, N.; Seydou, M.; Rahali, S. Adsorption behavior of barium ions onto ZnO surfaces: Experiments associated with DFT calculations. *J. Mol. Struct.* **2020**, *1223*, 128991. [CrossRef]
12. Pishnamazi, M.; Khan, A.; Kurniawan, T.A.; Sanaeepur, H.; Albadarin, A.B.; Soltani, R. Adsorption of dyes on multifunctionalized nano-silica KCC-1. *J. Mol. Liq.* **2021**, *338*, 116573. [CrossRef]
13. Ghoniem, M.G.; Ali, F.A.M.; Abdulkhair, B.Y.; Elamin, M.R.A.; Alqahtani, A.M.; Rahali, S.; Ben Aissa, M.A. Highly Selective Removal of Cationic Dyes from Wastewater by MgO Nanorods. *Nanomaterials* **2022**, *12*, 1023. [CrossRef] [PubMed]
14. Sharma, G.; Kumar, A.; Naushad, M.; Thakur, B.; Vo, D.-V.N.; Gao, B.; Al-Kahtani, A.A.; Stadler, F.J. Adsorptional-photocatalytic removal of fast sulphon black dye by using chitin-cl-poly(itaconic acid-co-acrylamide)/zirconium tungstate nanocomposite hydrogel. *J. Hazard. Mater.* **2021**, *416*, 125714. [CrossRef]
15. Castaldi, M.; van Deventer, J.; Lavoie, J.M.; Legrand, J.; Nzihou, A.; Pontikes, Y.; Py, X.; Vandecasteele, C.; Vasudevan, P.T.; Verstraete, W. Progress and Prospects in the Field of Biomass and Waste to Energy and Added-Value Materials. *Waste Biomass-Valorization* **2017**, *8*, 1875–1884. [CrossRef]
16. Charii, H.; Boussetta, A.; Benali, K.; Essifi, K.; Mennani, M.; Benhamou, A.A.; El Zakhem, H.; Sehaqui, H.; El Achaby, M.; Grimi, N.; et al. Phosphorylated chitin from shrimp shell waste: A robust solution for cadmium remediation. *Int. J. Biol. Macromol.* **2024**, *268*, 131855. [CrossRef]
17. Ahmaruzzaman, M. Industrial wastes as low-cost potential adsorbents for the treatment of wastewater laden with heavy metals. *Adv. Colloid Interface Sci.* **2011**, *166*, 36–59. [CrossRef]
18. Azarian, M.H.; Sutapun, W. Biogenic calcium carbonate derived from waste shells for advanced material applications: A review. *Front. Mater.* **2022**, *9*, 1024977. [CrossRef]
19. Suwannasingha, N.; Kantavong, A.; Tunkijjanukij, S.; Aenglong, C.; Liu, H.-B.; Klaypradit, W. Effect of calcination temperature on structure and characteristics of calcium oxide powder derived from marine shell waste. *J. Saudi Chem. Soc.* **2022**, *26*, 101441. [CrossRef]
20. Montes-Atenas, G.; Valenzuela, F.; Montes-Atenas, G.; Valenzuela, F. Wastewater Treatment through Low Cost Adsorption Technologies. In *Physico-Chemical Wastewater Treatment and Resource Recovery*; Intech Open: Rijeka, Croatia, 2017. [CrossRef]
21. Li, A.; Ge, W.; Liu, L.; Qiu, G. Preparation, adsorption performance and mechanism of MgO-loaded biochar in wastewater treatment: A review. *Environ. Res.* **2022**, *212*, 113341. [CrossRef]
22. Cadman, J.; Zhou, S.; Chen, Y.; Li, Q. Cuttlebone: Characterisation, application and development of biomimetic materials. *J. Bionic Eng.* **2012**, *9*, 367–376. [CrossRef]
23. Darwish, A.S.; Osman, D.I.; Mohammed, H.A.; Attia, S.K. Cuttlefish bone biowaste for production of holey aragonitic sheets and mesoporous mayenite-embedded Ag_2CO_3 nanocomposite: Towards design high-performance adsorbents and visible-light photocatalyst for detoxification of dyes wastewater and waste oil recovery. *J. Photochem. Photobiol. A: Chem.* **2021**, *421*, 113523. [CrossRef]
24. Reinares-Fisac, D.; Veintemillas-Verdaguer, S.; Fernández-Díaz, L. Conversion of biogenic aragonite into hydroxyapatite scaffolds in boiling solutions. *CrystEngComm* **2016**, *19*, 110–116. [CrossRef]
25. Venkatesan, J.; Rekha, P.D.; Anil, S.; Bhatnagar, I.; Sudha, P.N.; Dechsakulwatana, C.; Kim, S.-K.; Shim, M.S. Hydroxyapatite from Cuttlefish Bone: Isolation, Characterizations, and Applications. *Biotechnol. Bioprocess Eng.* **2018**, *23*, 383–393. [CrossRef]
26. Kim, B.-S.; Kang, H.J.; Yang, S.-S.; Lee, J. Comparison of in vitro and in vivo bioactivity: Cuttlefish-bone-derived hydroxyapatite and synthetic hydroxyapatite granules as a bone graft substitute. *Biomed. Mater.* **2014**, *9*, 025004. [CrossRef]
27. Minakshi, M.; Visbal, H.; Mitchell, D.R.G.; Fichtner, M. Bio-waste chicken eggshells to store energy. *Dalton Trans.* **2018**, *47*, 16828–16834. [CrossRef] [PubMed]
28. Tagar, U.; Volpe, M.; Messineo, A.; Volpe, R. Highly ordered CaO from cuttlefish bone calcination for the efficient adsorption of methylene blue from water. *Front. Chem.* **2023**, *11*, 1132464. [CrossRef] [PubMed]
29. Xia, H.; Chen, L.; Fang, Y. Highly Efficient Removal of Congo red from Wastewater by Nano-Cao. *Sep. Sci. Technol.* **2013**, *48*, 2681–2687. [CrossRef]
30. Mahmoud, H.R.; El-Molla, S.A.; Saif, M. Improvement of physicochemical properties of Fe_2O_3/MgO nanomaterials by hydrothermal treatment for dye removal from industrial wastewater. *Powder Technol.* **2013**, *249*, 225–233. [CrossRef]
31. Said, R.B.; Rahali, S.; Aissa, M.A.B.; Albadri, A.; Modwi, A. Uptake of BF Dye from the Aqueous Phase by CaO-g-C_3N_4 Nanosorbent: Construction, Descriptions, and Recyclability. *Inorganics* **2023**, *11*, 44. [CrossRef]
32. Liu, N.; Wu, Y.; Sha, H. Magnesium oxide modified diatomite waste as an efficient adsorbent for organic dye removal: Adsorption performance and mechanism studies. *Sep. Sci. Technol.* **2019**, *55*, 234–246. [CrossRef]
33. Chamack, M.; Mahjoub, A.; Hosseinian, A. Facile synthesis of nanosized MgO as adsorbent for removal of congored dye from wastewate. *Nanochemistry Res.* **2018**, *3*, 85–91.
34. Hu, J.; Song, Z.; Chen, L.; Yang, H.; Li, J.; Richards, R. Adsorption properties of MgO(111) nanoplates for the dye pollutants from wastewater. *J. Chem. Eng. Data* **2010**, *55*, 3742–3748. [CrossRef]
35. Uko, C.A.; Tijani, J.O.; Abdulkareem, S.A.; Mustapha, S.; Egbosiuba, T.C.; Muzenda, E. Adsorptive properties of MgO/WO_3 nanoadsorbent for selected heavy metals removal from indigenous dyeing wastewater. *Process. Saf. Environ. Prot.* **2022**, *162*, 775–794. [CrossRef]
36. Toamah, W.O.; Fadhil, A.K. Preparation of nanoparticles from CaO and use it for removal of chromium (II), and mercury (II) from aqueous solutions. *J. Phys. Conf. Ser.* **2019**, *1234*, 012086. [CrossRef]

37. Gu, H.; Lin, W.; Sun, S.; Wu, C.; Yang, F.; Ziwei, Y.; Chen, N.; Ren, J.; Zheng, S. Calcium oxide modification of activated sludge as a low-cost adsorbent: Preparation and application in Cd(II) removal. *Ecotoxicol. Environ. Saf.* **2020**, *209*, 111760. [CrossRef]
38. Shakerian, K.; Esmaeili, H. Synthesis of CaO/Fe_3O_4 magnetic composite for the removal of Pb(II) and Co(II) from synthetic wastewater. *J. Serbian Chem. Soc.* **2018**, *83*, 237–249. [CrossRef]
39. El-Dafrawy, S.M.; Youssef, H.; Toamah, W.; El-Defrawy, M. Synthesis of nano-CaO particles and its application for the removal of copper (II), Lead (II), cadmium (II) and iron (III) from aqueous solutions. *Egypt. J. Chem.* **2015**, *58*, 579–589.
40. Kasirajan, R.; Bekele, A.; Girma, E. Adsorption of lead (Pb-II) using CaO-NPs synthesized by solgel process from hen eggshell: Response surface methodology for modeling, optimization and kinetic studies. *South Afr. J. Chem. Eng.* **2022**, *40*, 209–229. [CrossRef]
41. Zhou, K.; Wu, B.; Su, L.; Gao, X.; Chai, X.; Dai, X. Development of nano-CaO_2-coated clinoptilolite for enhanced phosphorus adsorption and simultaneous removal of COD and nitrogen from sewage. *Chem. Eng. J.* **2017**, *328*, 35–43.
42. Habiby, S.R.; Esmaeili, H.; Foroutan, R. Magnetically modified MgO nanoparticles as an efficient adsorbent for phosphate ions removal from wastewater. *Sep. Sci. Technol.* **2019**, *55*, 1910–1921. [CrossRef]
43. Cheng, Y.; Xie, Q.; Wu, Z.; Ji, L.; Li, Y.; Cai, Y.; Jiang, P.; Yu, B. Mechanistic insights into the selective adsorption of phosphorus from wastewater by MgO(100)-functionalized cellulose sponge. *Sci. Total Environ.* **2023**, *868*, 161646. [CrossRef] [PubMed]
44. Shirazinezhad, M.; Faghihinezhad, M.; Baghdadi, M.; Ghanbari, M. Phosphate removal from municipal effluent by a porous MgO-expanded graphite composite as a novel adsorbent: Evaluation of seawater as a natural source of magnesium ions. *J. Water Process Eng.* **2021**, *43*, 102232. [CrossRef]
45. Chen, W.; Wu, Y.; Xie, Z.; Li, Y.; Tang, W.; Yu, J. Calcium hydroxide recycled from waste eggshell resources for the effective recovery of fluoride from wastewater. *RSC Adv.* **2022**, *12*, 28264–28278. [CrossRef] [PubMed]
46. Shamraiz, U.; Ahmad, Z.; Raza, B.; Badshah, A.; Ullah, S.; Nadeem, M.A. CaO-promoted graphene-supported palladium nanocrystals as a universal electrocatalyst for direct liquid fuel cells. *ACS Appl. Mater. Interfaces* **2020**, *12*, 4396–4404. [CrossRef] [PubMed]
47. Kaedi, F.; Yavari, Z.; Noroozifar, M.; Saravani, H. Promoted electrocatalytic ability of the Pd on doped Pt in NiO-MgO solid solution toward methanol and ethanol oxidation. *J. Electroanal. Chem.* **2018**, *827*, 204–212. [CrossRef]
48. Mahendiran, C.; Rajesh, D.; Maiyalagan, T.; Prasanna, K. Pd Nanoparticles-Supported Carbon Nanotube-Encapsulated NiO/MgO Composite as an Enhanced Electrocatalyst for Ethanol Electrooxidation in Alkaline Medium. *ChemistrySelect* **2017**, *2*, 11438–11444. [CrossRef]
49. Li, N.; Zeng, Y.-X.; Chen, S.; Xu, C.-W.; Shen, P.-K. Ethanol oxidation on Pd/C enhanced by MgO in alkaline medium. *Int. J. Hydrogen Energy* **2014**, *39*, 16015–16019. [CrossRef]
50. Mahendiran, C.; Maiyalagan, T.; Scott, K.; Gedanken, A. Synthesis of a carbon-coated NiO/MgO core/shell nanocomposite as a Pd electro-catalyst support for ethanol oxidation. *Mater. Chem. Phys.* **2011**, *128*, 341–347. [CrossRef]
51. Xu, C.; Shen, P.K.; Ji, X.; Zeng, R.; Liu, Y. Enhanced activity for ethanol electrooxidation on Pt–MgO/C catalysts. *Electrochem. Commun.* **2005**, *7*, 1305–1308. [CrossRef]
52. Eisa, T.; Mohamed, H.O.; Choi, Y.-J.; Park, S.-G.; Ali, R.; Abdelkareem, M.A.; Oh, S.-E.; Chae, K.-J. Nickel nanorods over nickel foam as standalone anode for direct alkaline methanol and ethanol fuel cell. *Int. J. Hydrogen Energy* **2019**, *45*, 5948–5959. [CrossRef]
53. Khouchaf, A.; Takky, D.; Chbihi, M.E.; Benmokhtar, S. Electrocatalytic Oxidation of Methanol on Glassy Carbon Electrode Modified by Metal Ions (Copper and Nickel) Dispersed into Polyaniline Film. *J. Mater. Sci. Chem. Eng.* **2016**, *4*, 97–105. [CrossRef]
54. Mohamed, H.F.M.; E Abdel-Hady, E.; Hmamm, M.F.M.; Ibrahim, M.; Ahmed, H.; Mondy, M.; Yehia, H. A promising fuel cell catalyst using non-precious metal oxide. *IOP Conf. Ser. Mater. Sci. Eng.* **2018**, *464*, 012002. [CrossRef]
55. Gil, A. Challenges on waste-to-energy for the valorization of industrial wastes: Electricity, heat and cold, bioliquids and biofuels. *Environ. Nanotechnol. Monit. Manag.* **2022**, *17*, 100615. [CrossRef]
56. Maina, S.; Kachrimanidou, V.; Koutinas, A. A roadmap towards a circular and sustainable bioeconomy through waste valorization. *Curr. Opin. Green Sustain. Chem.* **2017**, *8*, 18–23. [CrossRef]
57. Seriño, M.N.V. Diversification of nonhydro renewable energy sources in developing countries. *Energy Ecol. Environ.* **2018**, *3*, 317–329. [CrossRef]
58. Huang, H.; Sun, D.; Wang, X. Low-Defect MWNT–Pt Nanocomposite as a High Performance Electrocatalyst for Direct Methanol Fuel Cells. *J. Phys. Chem. C* **2011**, *115*, 19405–19412. [CrossRef]
59. Zhao, J.; Zhang, L.; Chen, T.; Yu, H.; Zhang, L.; Xue, H.; Hu, H. Supercritical Carbon-Dioxide-Assisted Deposition of Pt Nanoparticles on Graphene Sheets and Their Application as an Electrocatalyst for Direct Methanol Fuel Cells. *J. Phys. Chem. C* **2012**, *116*, 21374–21381. [CrossRef]
60. Qiu, J.-D.; Wang, G.-C.; Liang, R.-P.; Xia, X.-H.; Yu, H.-W. Controllable Deposition of Platinum Nanoparticles on Graphene as an Electrocatalyst for Direct Methanol Fuel Cells. *J. Phys. Chem. C* **2011**, *115*, 15639–15645. [CrossRef]
61. Mehek, R.; Iqbal, N.; Noor, T.; Nasir, H.; Mehmood, Y.; Ahmed, S. Novel Co-MOF/Graphene Oxide Electrocatalyst for Methanol Oxidation. *Electrochim. Acta* **2017**, *255*, 195–204. [CrossRef]
62. Zhang, X.; Guo, A.; Ma, X.; Du, H.; Yan, L.; Hou, F.; Liu, J. Cuttlefish-Bone-Structure-like Lamellar Porous Fiber-Based Ceramics with Enhanced Mechanical Performances. *ACS Appl. Mater. Interfaces* **2023**, *15*, 13121–13130. [CrossRef]
63. Ferro, A.C.; Guedes, M. Mechanochemical synthesis of hydroxyapatite using cuttlefish bone and chicken eggshell as calcium precursors. *Mater. Sci. Eng. C* **2019**, *97*, 124–140. [CrossRef]

64. Henggu, K.U.; Ibrahim, B.; Suptijah, P. Hidroksiapatit dari cangkang sotong sebagai sediaan biomaterial perancah tulang. *J. Pengolah. Has. Perikan. Indones.* **2019**, *22*, 1–13.
65. Lee, S.J.; Lee, Y.C.; Yoon, Y.S. Characteristics of calcium phosphate powders synthesized from cuttlefish bone and phosphoric acid. *J. Ceram. Process. Res.* **2007**, *8*, 427–430.
66. Wang, T.; Hu, Y.-H.; Chen, L.; Wang, X.-J. Luminescence properties and energy transfer of a red-emitting $Ca_3(PO_4)_2$:Sm^{3+}, Eu^{3+} phosphor. *J. Mater. Sci. Mater. Electron.* **2015**, *26*, 5360–5367. [CrossRef]
67. Cestari, F.; Agostinacchio, F.; Galotta, A.; Chemello, G.; Motta, A.; Sglavo, V.M. Nano-hydroxyapatite derived from biogenic and bioinspired calcium carbonates: Synthesis and in vitro bioactivity. *Nanomaterials* **2021**, *11*, 264. [CrossRef]
68. Sharmila, P.P.; Tharayil, N.J. Chemically synthesized nano composite (Zinc/Magnesium) Oxide for tunable band gap devices. *IOP Conf. Ser. Mater. Sci. Eng.* **2015**, *73*, 01201. [CrossRef]
69. Jannah, Z.; Mubarok, H.; Syamsiyah, F.; Putri, A.A.H.; Rohmawati, L. Preparation of Calcium Carbonate (from Shell-fish)/Magnesium Oxide Composites as an Antibacterial Agent. *IOP Conf. Ser. Mater. Sci. Eng.* **2018**, *367*, 012005. [CrossRef]
70. Nagalakshmi, G.; Nandeesh, I.; Yallur, B.C.; Adimule, V.; Batakurki, S. Synthesis and Optical Properties of Copper Terephthalate Metal Organic Frame Works. *Eng. Chem.* **2023**, *2*, 3–11. [CrossRef]
71. Jeyakumar, S.J.; Sindhya, A.; Jothibas, M. A comparative study of surface modified nanohydroxyapatite using PVA polymer extracted from Seashells, Coral Skeletons and Eggshells for biomedical applications. *Surf. Interfaces* **2023**, *42*, 103401. [CrossRef]
72. Dhanaraj, K.; Suresh, G. Conversion of waste sea shell (*Anadara granosa*) into valuable nanohydroxyapatite (nHAp) for biomedical applications. *Vacuum* **2018**, *152*, 222–230. [CrossRef]
73. Poinern, G.E.; Brundavanam, R.; Le, T.; Djordjevic, S.; Prokic, M.; Fawcett, D. Thermal and ultrasonic influence in the formation of nanometer scale hydroxyapatite bio-ceramic. *Int. J. Nanomed.* **2011**, *6*, 2083–2095. [CrossRef] [PubMed]
74. Balu, S.; Sundaradoss, M.V.; Andra, S.; Jeevanandam, J. Facile biogenic fabrication of hydroxyapatite nanorods using cuttlefish bone and their bactericidal and biocompatibility study. *Beilstein J. Nanotechnol.* **2020**, *11*, 285–295. [CrossRef]
75. Sun, L.; Chow, L.C.; Frukhtbeyn, S.A.; Bonevich, J.E. Preparation and Properties of Nanoparticles of Calcium Phosphates With Various Ca/P Ratios. *J. Res. Natl. Inst. Stand. Technol.* **2010**, *115*, 243–255. [CrossRef]
76. Kuriakose, T.; Kalkura, S.; Palanichamy, M.; Arivuoli, D.; Dierks, K.; Bocelli, G.; Betzel, C. Synthesis of stoichiometric nano crystalline hydroxyapatite by ethanol-based sol–gel technique at low temperature. *J. Cryst. Growth* **2004**, *263*, 517–523. [CrossRef]
77. Leontie, L.; Doroftei, C.; Carlescu, A. Nanocrystalline iron manganite prepared by sol–gel self-combustion method for sensor applications. *Appl. Phys. A* **2018**, *124*, 750. [CrossRef]
78. Emami, N.; Farhadian, M.; Solaimany Nazar, A.R.; Tangestaninejad, S. Adsorption of cefixime and lamotrigine on HKUST-1/ZIF-8 nanocomposite: Isotherms, kinetics models and mechanism. *Int. J. Environ. Sci. Technol.* **2023**, *20*, 1645–1672. [CrossRef]
79. Moridi, A.; Sabbaghi, S.; Rasouli, J.; Rasouli, K.; Hashemi, S.A.; Chiang, W.; Mousavi, S.M. Removal of Cefixime from Wastewater Using a Superb nZVI/Copper Slag Nanocomposite: Optimization and Characterization. *Water* **2023**, *15*, 1819. [CrossRef]
80. Wang, S.; Ariyanto, E. Competitive adsorption of malachite green and Pb ions on natural zeolite. *J. Colloid Interface Sci.* **2007**, *314*, 25–31. [CrossRef]
81. Fabryanty, R.; Valencia, C.; Soetaredjo, F.E.; Putro, J.N.; Santoso, S.P.; Kurniawan, A.; Ju, Y.-H.; Ismadji, S. Removal of crystal violet dye by adsorption using bentonite–alginate composite. *J. Environ. Chem. Eng.* **2017**, *5*, 5677–5687. [CrossRef]
82. Abdel-Hady, E.; Mahmoud, R.; Hafez, S.H.; Mohamed, H.F. Hierarchical ternary ZnCoFe layered double hydroxide as efficient adsorbent and catalyst for methanol electrooxidation. *J. Mater. Res. Technol.* **2022**, *17*, 1922–1941. [CrossRef]
83. Langmuir, I. The adsorption of gases on plane surfaces of glass, mica and platinum. *J. Am. Chem. Soc.* **1918**, *40*, 1361–1403. [CrossRef]
84. Nagy, B.; Mânzatu, C.; Măicăneanu, A.; Indolean, C.; Barbu-Tudoran, L.; Majdik, C. Linear and nonlinear regression analysis for heavy metals removal using Agaricus bisporus macrofungus. *Arab. J. Chem.* **2017**, *10*, S3569–S3579. [CrossRef]
85. Dubinin, M.M. The Potential Theory of Adsorption of Gases and Vapors for Adsorbents with Energetically Nonuniform Surfaces. *Chem. Rev.* **1960**, *60*, 235–241. [CrossRef]
86. Sips, R. Combined form of Langmuir and Freundlich equations. *J. Chem. Phys.* **1948**, *16*, 490–495. [CrossRef]
87. Toth, J. State equation of the solid-gas interface layers. *Acta Chim. Hung.* **1971**, *69*, 311–328.
88. Redlich, O.; Peterson, D.L. A Useful Adsorption Isotherm. *J. Phys. Chem.* **1959**, *63*, 1024. [CrossRef]
89. Vilela, P.B.; Dalalibera, A.; Duminelli, E.C.; Becegato, V.A.; Paulino, A.T. Adsorption and removal of chromium (VI) contained in aqueous solutions using a chitosan-based hydrogel. *Environ. Sci. Pollut. Res.* **2018**, *26*, 28481–28489. [CrossRef]
90. Baudu, M. Etude des interactions solutes-fibres de charbon actif: Applications et regeneration. Ph.D. Thesis, Université de Rennes 1, Rennes, France, 1990.
91. Majd, M.M.; Kordzadeh-Kermani, V.; Ghalandari, V.; Askari, A.; Sillanpää, M. Adsorption isotherm models: A comprehensive and systematic review (2010–2020). *Sci. Total Environ.* **2021**, *812*, 151334. [CrossRef]
92. Ayawei, N.; Ebelegi, A.N.; Wankasi, D. Modelling and Interpretation of Adsorption Isotherms. *J. Chem.* **2017**, *2017*, 3039817. [CrossRef]
93. Adebayo, M.A.; Areo, F.I. Removal of phenol and 4-nitrophenol from wastewater using a composite prepared from clay and Cocos nucifera shell: Kinetic, equilibrium and thermodynamic studies. *Resour. Environ. Sustain.* **2021**, *3*, 100020. [CrossRef]
94. Hu, Q.; Pang, S.; Wang, D. In-depth Insights into Mathematical Characteristics, Selection Criteria and Common Mistakes of Adsorption Kinetic Models: A Critical Review. *Sep. Purif. Rev.* **2021**, *51*, 281–299. [CrossRef]

95. Chahinez, H.-O.; Abdelkader, O.; Leila, Y.; Tran, H.N. One-stage preparation of palm petiole-derived biochar: Characterization and application for adsorption of crystal violet dye in water. *Environ. Technol. Innov.* **2020**, *19*, 100872. [CrossRef]
96. GadelHak, Y.; El-Azazy, M.; Shibl, M.F.; Mahmoud, R.K. Cost estimation of synthesis and utilization of nano-adsorbents on the laboratory and industrial scales: A detailed review. *Sci. Total Environ.* **2023**, *875*, 162629. [CrossRef]
97. Ajiboye, T.O.; Oyewo, O.A.; Onwudiwe, D.C. Adsorption and photocatalytic removal of Rhodamine B from wastewater using carbon-based materials. *FlatChem* **2021**, *29*, 100277. [CrossRef]
98. Han, Y.; Li, W.; Zhang, J.; Meng, H.; Xu, Y.; Zhang, X. Adsorption behavior of Rhodamine B on nanoporous polymers. *RSC Adv.* **2015**, *5*, 104915–104922. [CrossRef]
99. Hayeeye, F.; Sattar, M.; Chinpa, W.; Sirichote, O. Kinetics and thermodynamics of Rhodamine B adsorption by gelatin/activated carbon composite beads. *Colloids Surf. A Physicochem. Eng. Asp.* **2017**, *513*, 259–266. [CrossRef]
100. Sen, N.; Shefa, N.R.; Reza, K.; Shawon, S.M.A.Z.; Rahman, W. Adsorption of crystal violet dye from synthetic wastewater by ball-milled royal palm leaf sheath. *Sci. Rep.* **2024**, *14*, 5349. [CrossRef]
101. Postai, D.L.; Demarchi, C.A.; Zanatta, F.; Melo, D.C.C.; Rodrigues, C.A. Adsorption of rhodamine B and methylene blue dyes using waste of seeds of Aleurites Moluccana, a low cost adsorbent. *Alex. Eng. J.* **2016**, *55*, 1713–1723. [CrossRef]
102. Sultana, S.; Islam, K.; Hasan, A.; Khan, H.J.; Khan, M.A.R.; Deb, A.; Raihan, A.; Rahman, W. Adsorption of crystal violet dye by coconut husk powder: Isotherm, kinetics and thermodynamics perspectives. *Environ. Nanotechnol. Monit. Manag.* **2022**, *17*. [CrossRef]
103. Motahari, F.; Mozdianfard, M.R.; Salavati-Niasari, M. Synthesis and adsorption studies of NiO nanoparticles in the presence of H2acacen ligand, for removing Rhodamine B in wastewater treatment. *Process. Saf. Environ. Prot.* **2015**, *93*, 282–292. [CrossRef]
104. Al-Shahrani, S. Phenomena of Removal of Crystal Violet from Wastewater Using Khulays Natural Bentonite. *J. Chem.* **2020**, *2020*, 1–8. [CrossRef]
105. Geng, J.; Gu, F.; Chang, J. Fabrication of magnetic lignosulfonate using ultrasonic-assisted in situ synthesis for efficient removal of Cr(VI) and Rhodamine B from wastewater. *J. Hazard. Mater.* **2019**, *375*, 174–181. [CrossRef] [PubMed]
106. Muthukumaran, C.; Sivakumar, V.M.; Thirumarimurugan, M. Adsorption isotherms and kinetic studies of crystal violet dye removal from aqueous solution using surfactant modified magnetic nanoadsorbent. *J. Taiwan Inst. Chem. Eng.* **2016**, *63*, 354–362. [CrossRef]
107. Li, Q.; Tang, X.; Sun, Y.; Wang, Y.; Long, Y.; Jiang, J.; Xu, H. Removal of Rhodamine B from wastewater by modified Volvariella volvacea: Batch and column study. *RSC Adv.* **2015**, *5*, 25337–25347. [CrossRef]
108. Rani, S.; Chaudhary, S. Adsorption of methylene blue and crystal violet dye from waste water using Citrus limetta peel as an adsorbent. *Mater. Today Proc.* **2022**, *60*, 336–344. [CrossRef]
109. Mahmoud, R.; Mohamed, H.F.M.; Hafez, S.H.M.; Gadelhak, Y.M.; Abdel-Hady, E.E. Valorization of spent double substituted Co–Ni–Zn–Fe LDH wastewater nanoadsorbent as methanol electro-oxidation catalyst. *Sci. Rep.* **2022**, *12*, 19354. [CrossRef]
110. Mohamed, H.; Mahmoud, R.; Abdelwahab, A.; Farghali, A.A.; El-Ela, F.I.A.; Allah, A.E. Multifunctional ternary ZnMgFe LDH as an efficient adsorbent for ceftriaxone sodium and antimicrobial agent: Sustainability of adsorption waste as a catalyst for methanol electro-oxidation. *RSC Adv.* **2023**, *13*, 26069–26088. [CrossRef]
111. Kamal, W.; Mahmoud, R.; Allah, A.E.; Abdelwahab, A.; Taha, M.; Farghali, A.A. Insights into synergistic utilization of residual of ternary layered double hydroxide after oxytetracycline as a potential catalyst for methanol electrooxidation. *Chem. Eng. Res. Des.* **2022**, *188*, 249–264. [CrossRef]
112. Sharma, A.; Aggarwal, N.; Rastogi, S.; Choudhury, R.; Tripathi, S. Effectiveness of platelet-rich fibrin in the management of pain and delayed wound healing associated with established alveolar osteitis (dry socket). *Eur. J. Dent.* **2017**, *11*, 508–513. [CrossRef]
113. Gürses, A.; Doğar, Ç.; Yalçın, M.; Açıkyıldız, M.; Bayrak, R.; Karaca, S. The adsorption kinetics of the cationic dye, methylene blue, onto clay. *J. Hazard. Mater.* **2006**, *131*, 217–228. [CrossRef]
114. Senthilkumaar, S.; Varadarajan, P.; Porkodi, K.; Subbhuraam, C. Adsorption of methylene blue onto jute fiber carbon: Kinetics and equilibrium studies. *J. Colloid Interface Sci.* **2004**, *284*, 78–82. [CrossRef] [PubMed]
115. Rudzinski, W.; Plazinski, W. Kinetics of dyes adsorption at the solid−solution interfaces: A theoretical description based on the two-step kinetic model. *Environ. Sci. Technol.* **2008**, *42*, 2470–2475. [CrossRef] [PubMed]
116. Avrami, M. Kinetics of phase change. III: Granulation, phase change and microstructure. *J. Chem. Phys.* **1941**, *9*, 177–184. [CrossRef]